PHOTONIC SENSORS / Vol. 15, No. 4, 2025: 250433

Quadruple Plasmon-Induced Transparency Effect in Graphene Micro-Nano Structure and Its Applications for Switching, Sensing, and Slow Light

Zherui CUI[1], Kunhua WEN[1,2,3*], Haopeng LV[4*], Wenjie LIU[2,3,5], Yuesi YU[1],
Ruiling ZHANG[1], and Runming LIU[1]

[1] *School of Physics and Optoelectronic Engineering, Guangdong University of Technology, Guangzhou 510006, China*

[2] *Guangdong Provincial Key Laboratory of Information Photonics Technology, Guangdong University of Technology, Guangzhou 510006, China*

[3] *Key Laboratory of Photonic Technology for Integrated Sensing and Communication, Ministry of Education of the People's Republic of China, Guangdong University of Technology, Guangzhou 510006, China*

[4] *Experimental Teaching Department, Guangdong University of Technology, Guangzhou 510006, China*

[5] *School of Information Engineering, Guangdong University of Technology, Guangzhou 510006, China*

*Corresponding authors: Kunhua WEN and Haopeng LV　E-mails: khwen@gdut.edu.cn and lvhp2022@gdut.edu.cn

Abstract: A single-layer graphene structure is put forward to generate quadruple plasmon-induced transparency (PIT) at the terahertz frequency by coupling the bright-dark mode and bright-bright mode originated from five graphene strips. Based on the research on the electric field intensity of the PIT transparent window, it is suggested that intense fatal interference occurs among the bright and dark modes. The PIT reaction of the structure is analyzed and simulated with the coupled mode theory (CMT) and the finite difference time domain (FDTD) approach. Tunable multi-frequency switching is achieved under this quadruple transparency effect, since the maximum modulation depth (MD) is as high as 95% and the minimum insertion loss (IL) is 0.17 dB. Besides, the time delay and the group refractive index within the PIT windows can be up to 0.744 ps and 722, respectively. The proposed structure shows another fascinating ability to be sensitive to the nearby refractive index with the sensitivity of up to 0.91 THz/RIU. Therefore, this structure offers another novel thinking to design the multichannel switches, slow light instruments, and sensors in the terahertz band.

Keywords: Graphene; plasmon-induced transparency; multi-frequency switching; sensitivity; slow light

Citation: Zherui CUI, Kunhua WEN, Haopeng LV, Wenjie LIU, Yuesi YU, Ruiling ZHANG, *et al.* "Quadruple Plasmon-Induced Transparency Effect in Graphene Micro-Nano Structure and Its Applications for Switching, Sensing, and Slow Light," *Photonic Sensors*, 2025, 15(4): 250433.

1. Introduction

Graphene [1], a promising two-dimensional semiconductor material, exhibits remarkable characteristics such as exceptionally high carrier mobility and outstanding photoelectric properties [2], while graphene plasmons that can interact with carriers and substances have been widely developed in the fields of optical storages [3, 4], optical switches [5], optical sensors [6, 7], slow light

---

Received: 23 May 2024 / Revised: 30 August 2024

DOI: 10.1007/s13320-025-0764-2
Article type: Regular

devices [8–10], optical nano antennas [11], and quantum information processing devices [12]. More importantly, plasmon-induced transparency (PIT) [13] achieved by the graphene metamaterial structure displays a highly controllable advantage through manipulation of the Fermi level in graphene.

Actually, PIT resembles the phenomenon of electromagnetically induced transparency in atomic systems, but can be conveniently realized by using nano graphene structures [14], and has been extensively reported. The single-PIT [15, 16], double-PIT [17–19], or triple-PIT [20–23] can be obtained in the single-layer structures. However, it is rarely discussed about quadruple-PIT by multiple coupling modes. What is more, it is found that when we use graphene as a metamaterial to generate PIT, photoelectric switches [24–27] and photoelectric sensors [28, 29] can be designed on the basis of the dynamic regulation of the gate voltage, associated with the slow light effect [30]. It can be obviously considered that the multiple-PIT can possess more transparent windows for those integrated applications [31]. Consequently, it is interestingly to develop the multi-frequency PIT effect.

A monolayer graphene structure made up of five graphene strips is proposed in this paper. It is found that the graphene layer located between the silicon and the silica sandwich shows a more stable phenomenon [32]. First, an upper double-vertically parallel graphene (UVPG) strip and a single upper transverse graphene (UTG) strip generate a PIT transparent window at 3.305 15 THz because of the bright-dark mode coupling effect. After adding a single lower transverse graphene strip (LTG) as a bright mode, the bright-dark-bright mode coupling effect with the UVPG, UTG, and LTG is performed again. Finally, a lower vertical short graphene (LVSG) strip as the dark mode is added, and it will be coupled with the UVPG, UTG, and LTG. However, due to the particularity of the structural position of the LTG and LVSG, the coupling effect will occur in the T-shaped structure formed by the LTG and LVSG, which shows a triple bright mode in the 1 THz to 7 THz band, leading to the quadruple PIT effect under the above conditions. Through controlling its Fermi level, we can change the effect of this graphene structure without varying its geometry. The coupled mode theory (CMT) and finite difference time domain (FDTD) approach are the mainly methods adopted for the analysis and simulation, and their results are greatly uniform. The graphene structure model shows good future in the realms of optical switching, sensing, and slow light area.

2. Design and analysis of structure

The three-dimensional (3D) representation of the graphene structure diagram is depicted in Fig. 1. A regularly distributed single-layer graphene metamaterial can be observed along both the x and y axes within the x-y plane. In addition, the interlayer is between a silica substrate which is 0.1 μm thick and a silicon substrate which is 0.2 μm thick. A linear polarized plane incident light [33] is launched vertically on the whole structure along the z axis direction, and plasmon excitation situation occurs in the graphene structure. According to Fig. 1, there are five graphene strips on the silicon substrate. The UVPG is located on the top of the silicon's surface, connecting to the UTG. The LTG is between the UTG and LVSG. The single graphene layer is 1 nm thick. Geometric coefficients are: S_1=6 μm, S_2=6 μm, S_3=2.4 μm, S_4=2.6 μm, S_5=1 μm, S_6=2.8 μm, S_7=0.8 μm, S_8=2 μm, S_9=0.8 μm, S_{10}=3.8 μm, S_{11}=0.5 μm, S_{12}=S_{13}=0.1 μm, and h=0.1 μm. The border conditions are periodically defined along the x and y axes, while a perfect matching layer will be utilized in the z axis. The chemical potential is set to 0.64 eV; the scattering rate is set to 0.000 18 eV; the conductivity scaling is set to 1; the temperature is set to 300 K. For the boundary conditions, the x and y axes are subjected to periodic definitions, and perfectly matched layers (PMLs) are employed in the z axis, which follow the standard default profile in the software. The simulation time is set to 15 000 fs, and the mesh step is set to 0.01 μm.

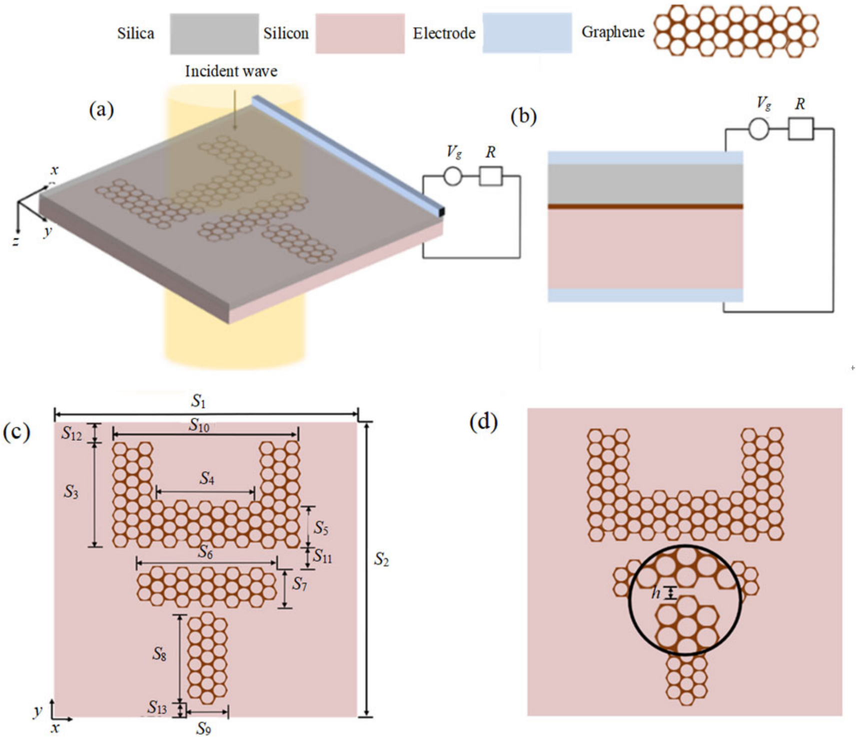

Fig. 1 Parameter of the designed structure: (a) the proposed is a metamaterial structure for graphene, depicted in a schematic diagram with 3D visualization, (b) the overhead perspective of the structural component, (c) the modulation diagram depicting the gate voltage, and (d) the partial enlargement of the graphene structure plan.

In the simulation of the entire process, we can ignore the thickness of the graphene because it is modeled in a two-dimensional (2D) surface. On basis of the Kubo [17, 34] (the formula is as follows), the complicated surface conductivity of the single-layer graphene includes the inter-band part and the intra-band part, σ^{inter} and σ^{intra}:

$$\sigma_g(\omega, E_f, \tau, T) = \sigma^{\text{intra}} + \sigma^{\text{inter}}$$
$$= \frac{2e^2 k_B T}{\pi\hbar^2}\frac{\mathrm{i}}{\omega + \mathrm{i}\tau^{-1}}\ln\left[2\cosh\left(\frac{E_f}{2k_B T}\right)\right] + \frac{e^2}{4\hbar^2}\left[\frac{1}{2} + \frac{1}{\pi}\arctan\left(\frac{\hbar\omega - 2E_f}{2k_B T}\right) - \frac{\mathrm{i}}{2\pi}\ln\frac{(\hbar\omega + 2E_f)^2}{(\hbar\omega - 2E_f)^2 + 4(k_B T)^2}\right] \quad (1)$$

where i denotes the imaginary number, $\hbar$, k_B, e, τ, ω, T, and E_f are the Planck constant, Boltzmann constant, electron charge, relaxation time, photon angular frequency, room temperature (300 K), and Fermi level, respectively. Based on Pauli's exclusion theorem, the intra-band transition exerts a main effect at room temperature, but the inter-band transition is able to be neglected. Consequently, σ_g can be simplified after integration and re-written as

$$\sigma_g = \frac{\mathrm{i}e^2 E_f}{\pi\hbar^2\left(\omega + \mathrm{i}\tau^{-1}\right)}. \quad (2)$$

The carrier relaxation time τ can be expressed as $\tau=\mu E_f/(eV_F^2)$. Besides, the Fermi velocity V_F and the carrier mobility μ of the whole monolayer graphene are fixed to 10^{-6} m/s and 4 $\text{m}^2\cdot$(V/s), respectively. In order to further analyze the properties of graphene, it is necessary to calculate its propagation constant. The propagation constant β of the guided mode and the effective refractive index n_{eff} can be expressed as follows [1, 36]:

$$n_{\text{eff}} = \frac{\beta}{k_0} \quad (3)$$

where k_0 is free-space wavenumber, which can be defined as $k_0=2\pi/\lambda_0=\omega/c$.

Since the graphene layer is located between the silica substrate and the silicon substrate, the dispersion association of graphene can be interpreted by using Maxwell's equation, while the electromagnetic field's boundary conditions are illustrated as [35, 36]

$$\frac{\varepsilon_{\mathrm{Si}}}{\sqrt{\beta^2-\varepsilon_{\mathrm{Si}}k_0^2}}+\frac{\varepsilon_{\mathrm{SiO_2}}}{\sqrt{\beta^2-\varepsilon_{\mathrm{SiO_2}}k_0^2}}=-\frac{\mathrm{i}\sigma_g}{\omega\varepsilon_0} \qquad (4)$$

where k_0 is the wave numbers in the free space; ε_0 is the dielectric constant of vacuum; $\varepsilon_{\mathrm{SiO_2}}$ is the relative dielectric constant of $\mathrm{SiO_2}$, and the relative dielectric constant of Si is $\varepsilon_{\mathrm{Si}}$. The transmission spectra of the PIT effects are shown in Fig. 2. A horizontally polarized wave propagating along the opposite *z*-axis is exposed vertically to the array of graphene, and obvious interference effects are observed. According to the FDTD simulation results, the first PIT peak shown in Fig. 2(a) comes from the mutual effect with the dark mode generated by UVPG and the bright mode generated by UTG. In Fig. 2(a), a transmission dip in the transmission spectrum of the UTG structure is discovered, while the spectral transmittance of the UVPG structure is up to 90% in a broadband frequency scope. Therefore, it is considered that the mutual effect occurs between the UTG serving as the bright mode at f_1=2.209 6 THz and the UVPG acting as the dark mode at f_3=4.151 6 THz, and Fig. 3 reveals the electric field allocation. The distribution of the energy concentration at f_1 and f_3 can be observed in the electric field depicted in Fig. 3(a), specifically at the lower and upper extremities of the UVPG, respectively, while the electric field intensity at f_2=3.383 1 THz has almost no energy distribution in the UTG structure. The reason for this phenomenon is that the transmission in the integrated structure of the UVPG and UTG exceeds 90% at this frequency, which is in line with the PIT peak generated from the bright-dark mode coupling.

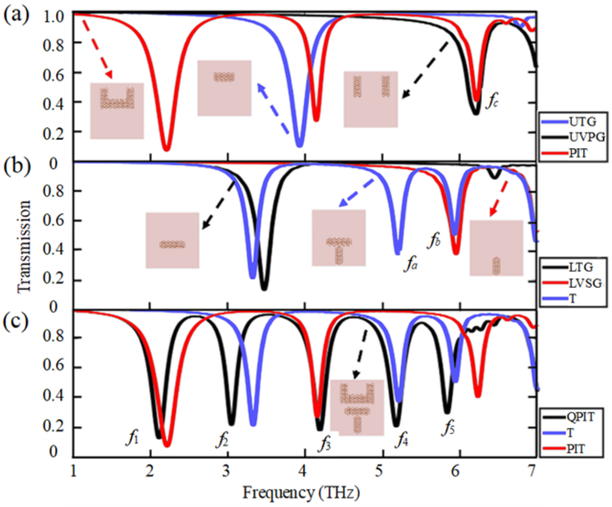

Fig 2 Transmission spectra of the various graphene structures with E_f=0.64 eV: (a) the generation process of single PIT, (b) the generation process of transmission of T-shape structure, and (c) the generation process of quadruple PIT.

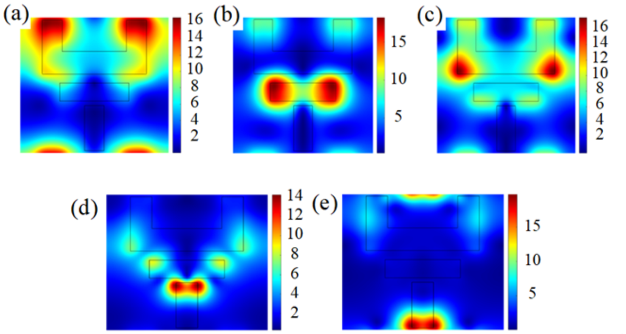

Fig. 3. Electric field intensity *E* is allocated at five resonance dips with E_f being 0.64 eV and the direction of the *x*-*y* plane: (a) f_1=2.107 55 THz, (b) f_2=3.044 02 THz, (c) f_3=4.187 59 THz, (d) f_4=5.172 09 THz, and (e) f_5=5.829 41 THz.

Furthermore, the structure LTG is added to the UVPG and UTG structures. According to the transmission spectrum and electric field distribution diagram, the LTG serves as a bright mode and is used to interact with the modes from the UVPG and UTG. The electric field intensity at f_2=3.044 0 THz displays the main distribution of energy on both sides of the LTG. According to the energy diagram of f_1, f_3, and f_4, the energy transfers among the co-coupled structure of the UVPG, UTG, and LTG, which proves that the addition of the LTG will affect the energy distribution of the overall structure, leading to a new transparent window. Therefore, it is interesting to find out that the law of the bright-dark mode or bright-bright mode interaction can result in the emergence of the PIT window.

Moreover, we also find that when the distance between the LTG and LVSG is maintained within a certain range, the two structures will form a new resonator while maintaining their original spectral transmission properties. Then, a bright mode with a transmission dip will be generated at f_a=5.205 1 THz in Fig. 2(b). The T-shaped structure formed by the LTG and LVSG can be regarded as a resonator capable of producing a triple-bright mode transmission dip in the 1 THz to 7 THz band. According to Fig. 2(c), the triple bright mode generated by the T-shaped structure will be coupled with the double PIT generated by the UVPG and UTG. The transmission dip at f_5=5.829 41 THz is generated by the superposition of the UVPG and LVSG energy at this frequency [inferred from the transmission spectrum frequencies at f_c=6.228 61 THz in Fig. 2(a) and f_b=5.934 47 THz in Fig. 2(b)]. In the field intensity allocations of the UVPG and LVSG structures, it is not difficult to see that the energy is concentrated at the same position, which also investigates the hypothesis of energy superposition. Observed from Figs. 2(a) and 2(b), the four structures of the UVPG, UTG, LTG, and LVSG are coupled together and four transparent windows are induced, resulting in a quadruple PIT phenomenon.

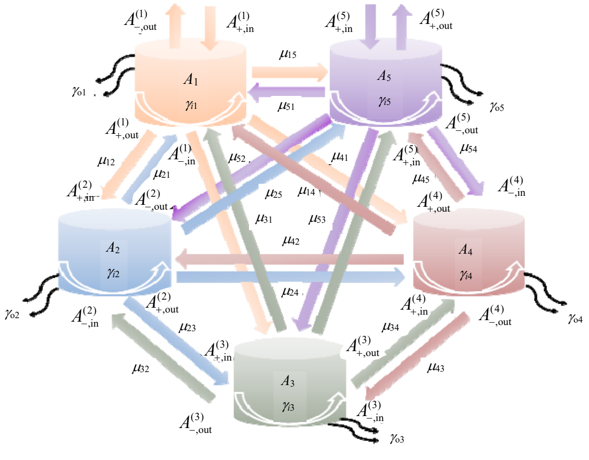

Fig. 4 Schematic diagram of CMT.

The CMT method is further used to investigate the performance of the quadruple PIT phenomenon, as shown in Fig. 4. The dark mode produced by the UVPG, the bright mode produced by the UTG, and the triple bright mode produced by the T-shaped structure are respectively recorded as A_1, A_2, A_3, A_4, and A_5. $A^{(n)}_{\pm,\text{out}}$ and $A^{(n)}_{\pm,\text{in}}$ represent the output and input waves of the nth resonator, where n (n=1, 2, 3, 4, and 5) and the subscript + and − indicates the positive and negative direction of the energy flow; the amplitudes of the five modes are expressed as a_1, a_2, a_3, a_4, and a_5, respectively, which can be obtained by [37, 38]:

$$\begin{pmatrix} \gamma_1 & -\mathrm{i}\mu_{12} & -\mathrm{i}\mu_{13} & -\mathrm{i}\mu_{14} & -\mathrm{i}\mu_{15} \\ -\mathrm{i}\mu_{21} & \gamma_2 & -\mathrm{i}\mu_{23} & -\mathrm{i}\mu_{24} & -\mathrm{i}\mu_{25} \\ -\mathrm{i}\mu_{31} & -\mathrm{i}\mu_{32} & \gamma_3 & -\mathrm{i}\mu_{34} & -\mathrm{i}\mu_{35} \\ -\mathrm{i}\mu_{41} & -\mathrm{i}\mu_{42} & -\mathrm{i}\mu_{43} & \gamma_4 & -\mathrm{i}\mu_{45} \\ -\mathrm{i}\mu_{51} & -\mathrm{i}\mu_{52} & -\mathrm{i}\mu_{53} & -\mathrm{i}\mu_{54} & \gamma_5 \end{pmatrix} \begin{pmatrix} a_1 \\ a_2 \\ a_3 \\ a_4 \\ a_5 \end{pmatrix}$$

$$= \begin{pmatrix} -\gamma_{o1}^{1/2} & 0 & 0 & 0 & 0 \\ 0 & -\gamma_{o2}^{1/2} & 0 & 0 & 0 \\ 0 & 0 & -\gamma_{o3}^{1/2} & 0 & 0 \\ 0 & 0 & 0 & -\gamma_{o4}^{1/2} & 0 \\ 0 & 0 & 0 & 0 & -\gamma_{o5}^{1/2} \end{pmatrix} \begin{pmatrix} A^{(1)}_{+,\text{in}} + A^{(1)}_{-,\text{in}} \\ A^{(2)}_{+,\text{in}} + A^{(2)}_{-,\text{in}} \\ A^{(3)}_{+,\text{in}} + A^{(3)}_{-,\text{in}} \\ A^{(4)}_{+,\text{in}} + A^{(4)}_{-,\text{in}} \\ A^{(5)}_{+,\text{in}} + A^{(5)}_{-,\text{out}} \end{pmatrix} \quad (5)$$

where γ_n=(iω−iω_n−γ_{in}−γ_{on}) (n=1, 2, 3, 4, and 5), ω_n is the frequency of the angular nth mode, γ_{in}=ω_n/(2Q_{in}) is the nth mode of the interval loss coefficient, γ_{on}=ω_n/(2Q_{on}) represents the nth mode of the applied loss coefficient (that is, the nth external decay rate); $\mu_{m,n}$ (m, n=1, 2, 3, 4, and 5, m≠n) stands for the coupling coefficient between the five types. Q_{in} represents the internal quality loss element and Q_{on} represents the nth external quality loss element. The relation 1/Q_{tn}=1/Q_{in}+1/Q_{on} can be adopted to obtain the external loss mass factor, where Q_{tn}=f/Δf represents the total mass element of the nth mode (f means the resonance frequency and Δf is half of the maximum full width) and the expression: Q_{in}=Re(n_{eff})/Im(n_{eff}) [39] can be adopted to obtain Q_{in}, and Re(n_{eff}) and Im(n_{eff}) are calculated in Fig. 5. On basis of the principle of conserving energy, the association among the input and the output waves are interpreted by

$$A^{(n-1)}_{-,\text{in}} = A^{(n)}_{-,\text{out}} \mathrm{e}^{\mathrm{j}\phi_{n-1}} \quad (n = 2, 3, 4, \text{and } 5) \qquad (6a)$$

$$A^{(n+1)}_{+,\text{in}} = A^{(n)}_{+,\text{out}} \mathrm{e}^{\mathrm{j}\phi_{n}} \quad (n = 2, 3, \text{and } 4) \qquad (6b)$$

where ϕ is the phase of waves.

$$A_{\pm,\mathrm{out}}^{(n)} = A_{\pm,\mathrm{in}}^{(n)} - a_n\sqrt{1/\tau_{on}} \tag{7a}$$

$$A_{-,\mathrm{in}}^{(n)} = 0 \tag{7b}$$

where n=1, 2, 3, 4, and 5.

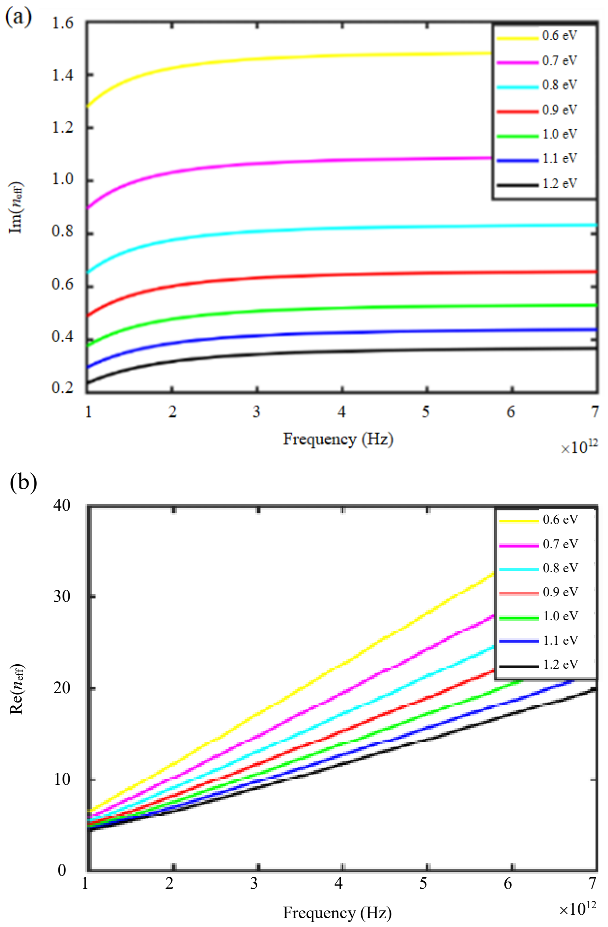

Fig. 5 Derivation basis of Q_{in}: (a) the imaginary part of the effective refractive index-the frequency-dependent variation in various Fermi levels and (b) the real part of the effective refractive index-the frequency-dependent variation in various Fermi levels.

Since A_1, A_2, A_3, A_4, and A_5 are located within the same plane, $\varphi_1=\varphi_2=\varphi_3=\varphi_4=\varphi_5=0$. Therefore, the energy transfer and feedback of the system can be summarized by the following equation [31, 40]:

$$t_1 = -\frac{t_\alpha}{t_\gamma} \tag{8}$$

$$t_2 = -\frac{t_\beta}{t_\gamma} \tag{9}$$

$$t_3 = \frac{LT+PS}{KP-LO} + \frac{IP-LM}{KP-LO}\cdot\frac{t_\alpha}{t_\gamma} + \frac{JP-LN}{KP-LO}\cdot\frac{t_\beta}{t_\gamma} \tag{10}$$

$$t_4 = \frac{O(LT+PS)-T(LO-KP)}{P(KP-LO)} + \frac{M(LO-KP)+O(IP-LM)}{P(KP-LO)}\cdot\frac{t_\alpha}{t_\gamma} + \frac{N(LO-KP)+O(JP-LN)}{P(KP-LO)}\cdot\frac{t_\beta}{t_\gamma} \tag{11}$$

$$\begin{aligned} t_\alpha = {} & [(HS+LR)(CH+DG)-(HQ-DR)(HK-GL)]\times \\ & [(KP-LO)(FL+HJ)-(JP-LN)(HK-GL)]+ \\ & [(LT+PS)(HK-GL)-(KP-LO)(HS+LR)]\times \\ & [(DF+BH)(HK-GL)+(CH+DG)(FL+JH)] \end{aligned} \tag{12}$$

$$\begin{aligned} t_\beta = {} & [(HQ-DR)(HK-GL)-(CH+DG)(HS+LR)]\times \\ & [(KP-LO)(EL+HI)-(IP-LM)(HK-GL)]- \\ & [(HS+LR)(KP-LO)-(LT+PS)(HK-GL)]\times \\ & [(AH-DE)(HK-GL)-(CH+DG)(EL+HI)] \end{aligned} \tag{13}$$

$$\begin{aligned} t_\gamma = {} & [(AH-DE)(HK-GL)-(CH+DG)(EL+HI)]\times \\ & [(KP-LO)(FL+JH)-(JP-LN)(HK-GL)]+ \\ & [(DF+BH)(HK-GL)+(CH+DG)(FL+JH)]\times \\ & [(KP-LO)(EL+HI)-(IP-LM)(HK-GL)] \end{aligned} \tag{14}$$

$$A = \gamma_1 x_{25} + x_{15}x_{21} \tag{15a}$$

$$B = \gamma_2 x_{15} + x_{12}x_{25} \tag{15b}$$

$$C = x_{15}x_{23} - x_{12}x_{25} \tag{15c}$$

$$D = x_{15}x_{24} - x_{14}x_{25} \tag{15d}$$

$$E = x_{25}x_{31} - x_{21}x_{35} \tag{15e}$$

$$F = \gamma_2 x_{35} + x_{25}x_{32} \tag{15f}$$

$$G = \gamma_3 x_{23} + x_{23}x_{35} \tag{15g}$$

$$H = x_{25}x_{34} - x_{24}x_{24} \tag{15h}$$

$$I = x_{35}x_{41} - x_{31}x_{45} \tag{15i}$$

$$J = x_{35}x_{42} - x_{32}x_{45} \tag{15j}$$

$$K = \gamma_3 x_{45} + x_{35}x_{43} \tag{15k}$$

$$L = \gamma_4 x_{35} + x_{34}x_{45} \tag{15l}$$

$$M = \gamma_5 x_{41} + x_{45}x_{51} \tag{15m}$$

$$N = \gamma_5 x_{42} + x_{45}x_{52} \tag{15n}$$

$$O = \gamma_5 x_{43} + x_{45}x_{53} \tag{15o}$$

$$P = \gamma_4\gamma_5 - x_{45}x_{54} \tag{15p}$$

$$Q = \sqrt{\frac{1}{\tau_{o1}}}x_{25} - \sqrt{\frac{1}{\tau_{o2}}}x_{15} \tag{16a}$$

$$R = \sqrt{\frac{1}{\tau_{o2}}}x_{35} - \sqrt{\frac{1}{\tau_{o3}}}x_{25} \tag{16b}$$

$$S=\sqrt{\frac{1}{\tau_{o3}}}x_{45}-\sqrt{\frac{1}{\tau_{o4}}}x_{35} \tag{16c}$$

$$T=\sqrt{\frac{1}{\tau_{o4}}}\gamma_{5}+\sqrt{\frac{1}{\tau_{o5}}}x_{45} \tag{16d}$$

$$x_{m,n}=\sqrt{\frac{1}{\tau_{om}\tau_{on}}}+\mathrm{i}\mu_{m,n} \tag{17}$$

where $m,n=1,2,3,4,$ and 5, $m\neq n$; τ_{om} and τ_{on} respectively represent the amplitudes of the output coupling coefficients of the *m*th and *n*th resonant channels.

Therefore, the theoretical quadruple PIT physical mechanism can thus be written as $T=|t|^2$.

3. Simulation outcomes and applications

The Fermi level E_f can be changed through varying the voltage V_g. The voltage V_g and the Fermi level are derived from the following mathematical relationship:

$$E_f=\hbar V_F\sqrt{\frac{\pi\varepsilon_0\varepsilon_{\mathrm{Si}}V_g}{de}} \tag{18}$$

where *d* stands for the thickness of the silicon substrate, ε_0, $\varepsilon_{\mathrm{Si}}$, *e*, and V_f refer to the vacuum permittivity, the relative permittivity of silicon, the electron charge, and the Fermi velocity; $\varepsilon_{\mathrm{Si}}=11.9$. Based on the Pauli exclusion theorem, because $\hbar\omega\ll 2E_f$ (ω means the photon angular frequency), the efforts of the intermediate value and the composite conductivity of the monolayer graphene in the terahertz scope can be ignored.

The transmission spectrum of the graphene metamaterial structure in the single-layer graphene is shown in Fig. 6 by adjusting E_f as 0.6 eV, 0.7 eV, 0.8 eV, 0.9 eV, 1.0 eV, 1.1 eV, and 1.2 eV. The numerical simulation outcomes of the FDTD simulation using the red curve conform to the theoretical calculation outcomes of the CMT using the black dashed line. The transmission spectrum will also red-shift or blue-shift as the Fermi level changes. The physical mechanism of resonance can interpret this situation.

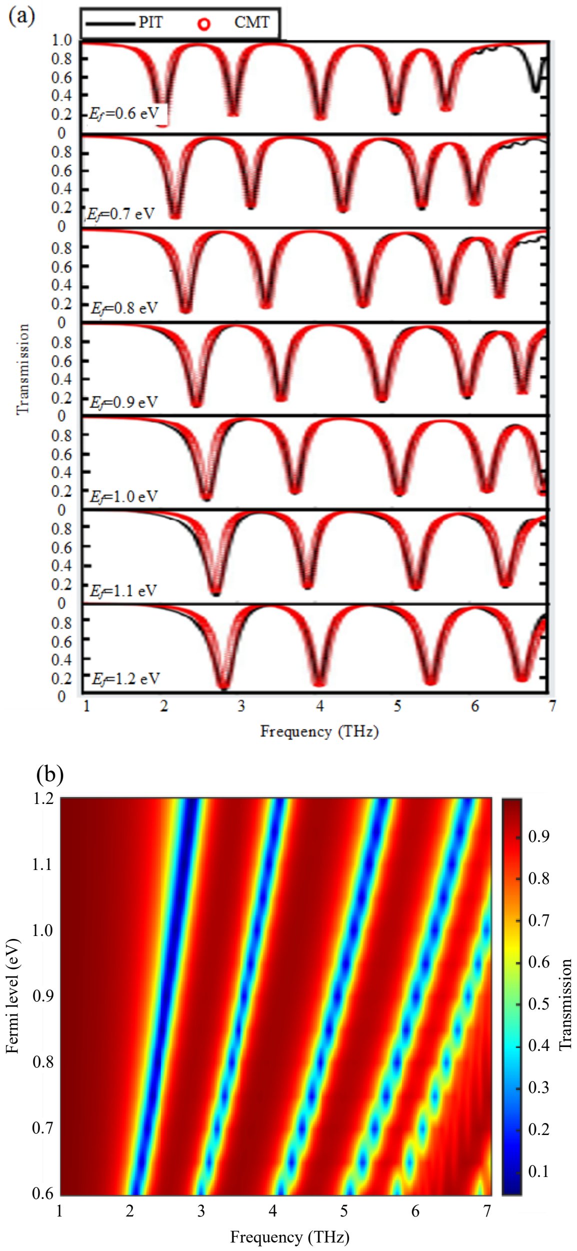

Fig. 6 Theoretical deduction process of quadruple transmission: (a) the transmission spectra of the graphene metamaterial structure exhibit variations corresponding to the modulation of the Fermi level and (b) the transmission spectra's 3D theoretical evolution is observed by adjusting the Fermi level within the range of 0.6 eV to 1.2 eV.

The MD [41] and IL [42] are the important factors to describe the optical switching effect, which can be obtained by

$$\mathrm{MD}=\frac{|T_{\mathrm{on}}-T_{\mathrm{off}}|}{T_{\mathrm{on}}}\times 100\% \tag{19}$$

$$\mathrm{IL}=-10\lg T_{\mathrm{on}}\ . \tag{20}$$

According to Fig. 7, the values of E_f are defined as 0.7 eV and 1.0 eV; 0.8 eV and 1.1 eV; 0.9 eV and 1.2 eV, respectively, and the MDs of the multi-channel switch get the maximum values of 92.3%, 93.7%, and 95%, which correspond to the minimum IL of 0.17 dB, 0.17 dB, and 0.18 dB. All the details are shown in Tables 1–4, respectively.

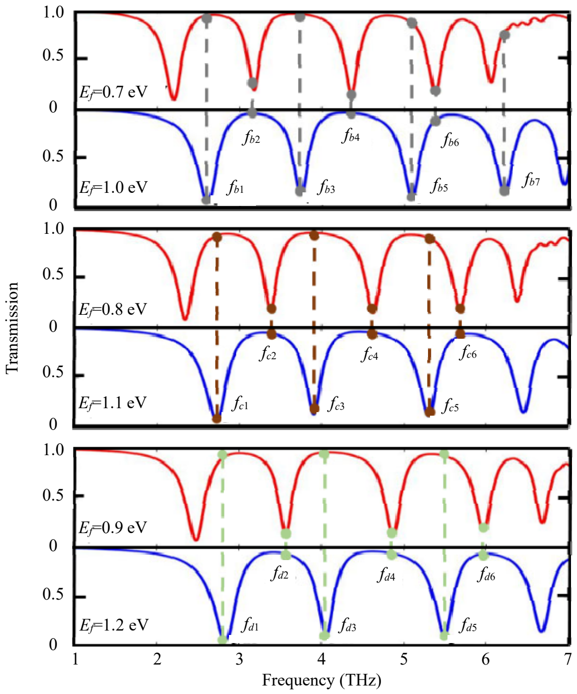

Fig. 7 Hexa-frequency synchronous switch when E_f=0.7 eV and 1.0 eV; 0.8 eV and 1.1 eV; 0.9 eV and 1.2 eV, where $f_{p,q}$ is the switching frequency (p=a, b, c, d; q=1, 2, 3, 4, 5, 6, or 7).

Table 1 MD and IL values are obtained for E_f of 0.7 eV and 1.0 eV.

Frequency (THz)	E_f=0.7 eV		E_f=1.0 eV			
	Tr*	On/off	Tr	On/off	MD (%)	IL (dB)
2.60	0.947	On	0.073	Off	92.3	0.24
2.20	0.109	Off	0.840	On	87.0	0.75
3.74	0.960	On	0.145	Off	85.1	0.18
4.36	0.166	Off	0.961	On	82.7	0.17
5.09	0.871	On	0.125	Off	85.6	0.56
5.37	0.193	Off	0.889	On	78.3	0.51
6.21	0.801	On	0.157	Off	80.4	0.96

*: Tr is transmission.

Besides, the refractive index sensing effect of the structure is examined through setting the surrounding dielectric material as the air (n=1.000), liquid carbon dioxide (n=1.200), water (n=1.330), 80% glucose solution (n=1.490), and benzene (n=1.550). By comparing the spectra, as refractive index grows, the transmission spectrum emerges a red-shift phenomenon. At room temperature, in addition to varying the Fermi energy level and the structural coefficients, we provide an alternative method to dynamically adjust the PIT by controlling the conductivity. Through the spectra of different refractive indices, the frequency of the transparent window decreases faster as the refractive index increases. The sensitivity is calculated by [46, 47]

$$S = \frac{\Delta f}{\Delta n}. \tag{21}$$

Table 2 MD and IL values are obtained for E_f of 0.8 eV and 1.1 eV.

Frequency (THz)	E_f=0.8 eV		E_f=1.1 eV			
	Tr	On/off	Tr	On/off	MD (%)	IL (dB)
2.72	0.937	On	0.059	Off	93.7	0.28
3.37	0.171	Off	0.946	On	82.0	0.24
3.90	0.961	On	0.129	Off	86.6	0.17
4.62	0.147	Off	0.949	On	84.5	0.23
5.29	0.911	On	0.115	Off	87.4	0.40
5.68	0.177	Off	0.927	On	81.1	0.33

Table 3 MD and IL values are obtained for E_f of 0.9 eV and 1.2 eV.

Frequency (THz)	E_f=0.9 eV		E_f=1.2 eV			
	Tr	On/off	Tr	On/off	MD (%)	IL (dB)
2.83	0.921	On	0.046	Off	95.0	0.36
3.56	0.153	Off	0.937	On	83.7	0.28
4.06	0.960	On	0.116	Off	88.1	0.18
4.86	0.132	Off	0.939	On	86.0	0.27
5.49	0.924	On	0.106	Off	88.5	0.34
5.96	0.167	Off	0.935	On	82.1	0.29

Table 4 MD and IL between our work and previously reported work.

Ref.	MD (%) maximum	IL (dB) minimum	Number of band for optical switch
[43]	93.7	5.3dB	5
[44]	94.5	0.13dB	3
[45]	81.4	/	3
This paper	95.0	0.17dB	6

According to the frequencies with different n in Table 5, the sensitivity of the five bands can be obtained as 0.53 THz/RIU, 0.55 THz/RIU, 0.91 THz/RIU, 0.50 THz/RIU, and 0.77 THz/RIU, as shown in Fig. 8. This represents that the structure can be adopted as a refractive-index sensor in the terahertz band. Table 6 shows the comparison of the sensitivity between our work and other published results, indicating that better performance is achieved in our devices.

Table 5 Values of frequencies and sensitivities with different *n*.

n	f_1 (THz)	f_2 (THz)	f_3 (THz)	f_4 (THz)	f_5 (THz)
1.00	2.107 55	3.044 02	4.187 59	5.172 09	5.829 41
1.20	1.993 50	2.929 96	4.004 50	5.073 04	5.679 34
1.33	1.924 46	2.857 93	3.884 44	5.007	5.577 29
1.49	1.846 42	2.773 89	3.740 37	4.928 96	5.454 23
1.55	1.816 41	2.740 87	3.686 34	4.898 95	5.406 2
Sensitivity (THz/RIU)	0.53	0.55	0.91	0.50	0.77

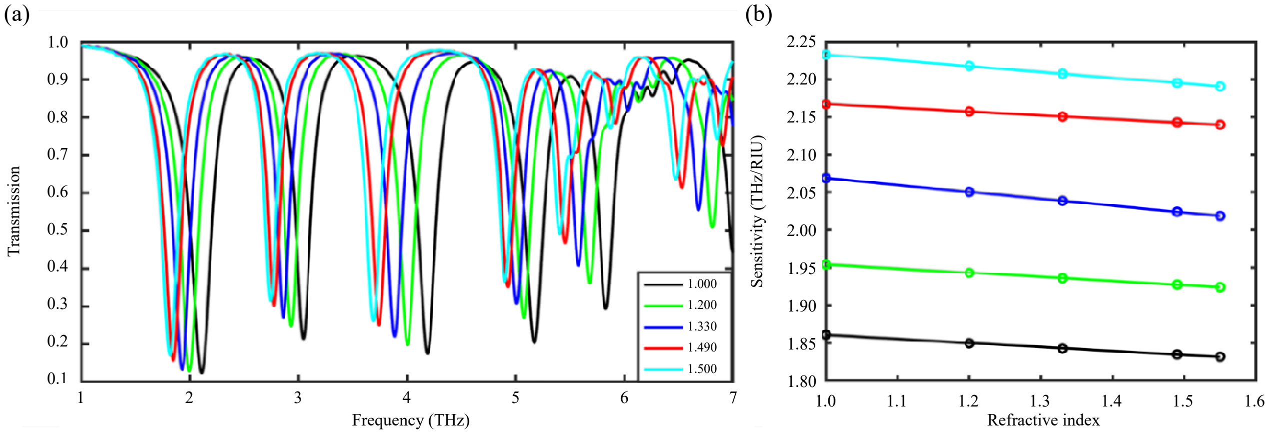

Fig. 8 Calculation of theoretical sensitivity: (a) transmission spectra of the PIT structure based on graphene are examined at various refractive indexes, with the Fermi level set at 0.64 eV and (b) relation between the resonant PIT valley and refractive index.

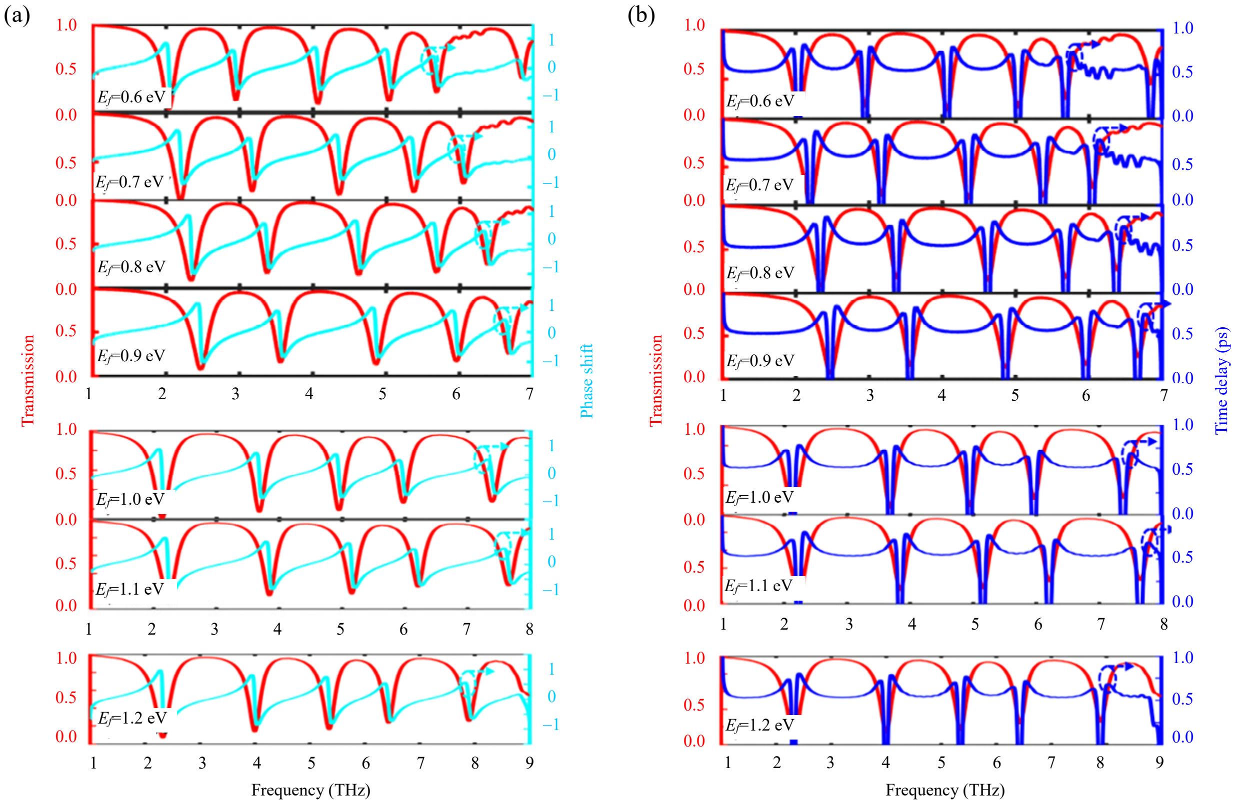

Fig. 9 Frequency-dependent: (a) the phase shift (the cyan line) and (b) time delay (the blue line) are observed as the Fermi level transmission varying from 0.6 eV to 1.2 eV. The corresponding transmission spectra are represented by the red line.

In addition, we modulate the Fermi level ranging from 0.6 eV to 1.2 eV in Fig. 9 which shows the development of the phase shift, time delay, and transmission spectra. According to Fig. 9, the solid cyan line is referred to the phase shift calculated mathematically. In one aspect, the transmission spectra plotted with the red solid line blue-shift as the Fermi level increases, and the phase shifts. In another aspect, the phase shift oscillates up and down with the growing frequency and the fixed Fermi level. It reaches its minimum value at the transmission dip. In addition, in the case of the wider transmission dip, the full width at half maximum (FWHM) and the phase shift will be larger. The phase shift reaches its maximum in the case of the fixed Fermi level at 1.2 eV. For one reason, as the Fermi level increasing, the slow light effect near each transmission dip is identical, the phase shift and Fermi level becoming more relevant. Figure 9(b) shows the PIT spectra and the group time delays, revealing a strong dispersion situation at the transmission dip. As the Fermi level grows, the maximum delay is achieved when the Fermi level is modulated within 0.6 eV–1.2 eV. Because of the blue shift, the value of the horizontal axis will be enlarged at 1.0 eV–1.2 eV. For a further intuitive display, the simulated results among different Fermi levels are compared in Tables 7 and 8. In the case of the fixed Fermi level at 0.8 eV, the largest time delay around the five transmission dips is 0.744 ps, 0.676 ps, 0.638 ps, 0.577 ps, and 0.528 ps, respectively. In the meantime, the related highest group refractive indices are 722, 675, 635, 579, and 552 at the five transmission dips, respectively, as shown in Table 9, which can be inferred from (22).

$$n_g = c\frac{\mathrm{d}k_0}{\mathrm{d}\omega} = \frac{c}{h}\frac{\mathrm{d}\theta}{\mathrm{d}\omega} \tag{22}$$

where g is 1, 2, 3, 4, and 5; θ is the azimuthal angle.

Therefore, it can be concluded that the graphene structures can obtain the largest time delay at 0.744 ps and the highest group refractive index is 722. More details about the group refractive index are shown in Table 9. The slow light role of this structure is relatively remarkable.

Table 6 Comparison of the sensitivity between our work and previously reported works.

Ref.	Materials	Sensitivity (THz/RIU)
[48]	Graphene (SiO_2)	0.19
[49]	NaCl and ethanol	0.583
[50]	Graphene (Si)	0.7
This paper	Graphene (SiO_2 and Si)	0.91

Table 7 Values of the phase shift with different Fermi levels.

Fermi level (eV)	Phaseshift_1	Phaseshift_2	Phaseshift_3	Phaseshift_4	Phaseshift_5
0.6	0.871	0.632	0.746	0.676	0.429
0.7	0.914	0.662	0.764	0.690	0.415
0.8	0.970	0.719	0.804	0.717	0.431
0.9	0.993	0.728	0.829	0.731	0.444
1.0	0.979	0.750	0.835	0.734	0.755
1.1	1.026	0.786	0.825	0.657	0.673
1.2	1.081	0.812	0.844	0.644	0.678

Table 8 Values of the delay with different Fermi levels.

Fermi level (eV)	Delay_1 (ps)	Delay_2 (ps)	Delay_3 (ps)	Delay_4 (ps)	Delay_5 (ps)
0.6	0.686	0.644	0.634	0.553	0.517
0.7	0.711	0.632	0.628	0.582	0.526
0.8	0.744	0.676	0.638	0.577	0.528
0.9	0.693	0.654	0.641	0.570	0.504
1.0	0.676	0.653	0.635	0.534	0.488
1.1	0.697	0.677	0.634	0.585	0.512
1.2	0.700	0.686	0.648	0.568	0.533

Table 9 Values of the index with different Fermi levels.

Fermi level (eV)	n_1	n_2	n_3	n_4	n_5
0.6	661	620	587	526	490
0.7	700	623	620	522	501
0.8	722	649	632	560	518
0.9	677	643	616	572	509
1.0	664	639	635	576	549
1.1	691	657	602	579	552
1.2	692	675	628	550	546

4. Conclusions

In conclusion, a new graphene structure, made up of four graphene strips to realize the quadruple PIT phenomenon in the terahertz band, has been proposed. FDTD and CMT methods are adopted to explore the PIT effect, which is investigated to be generated by the strong resonant disturbance among the dark and bright modes coupling. The multi-frequency synchronous optical switch with the highest MD up to 95% is achieved in the proposed structure. The index sensitivity is up to 0.91 THz/RIU, which can be investigated through varying the refractive indicator. Besides, the slow light effect is obtained as well. The largest group delay is 0.744 ps and the highest group refractive indicator is 722. Considering the design process, it is found that the configuration of this waveguide device may be a little complex, thus its manufacture process requirements and preparation cost is relatively high. There is still much room for improvement in this kind of graphene-based structures. Nevertheless, this terahertz multi-channel graphene structure presents innovative prospects for developing optical switches, sensors, and slow light equipment.

Acknowledgement

This work is supported by the National Natural Science Foundation of China (Grant Nos. 62175039, U2001601, 62275054, and 61975037); the Natural Science Foundation of Guangdong Province, China (Grant No. 2023A1515010206); the Guangzhou Science and Technology Plan Project, China (Grant No. 2025A04J5486); the 2021 Characteristic Innovation Research Project for University Teachers, China (Grant No. 2021DZXX21).

Declarations

Conflict of Interest The authors declare that they have no competing interests.

Permissions All the included figures, tables, or text passages that have already been published elsewhere have obtained the permission from the copyright owner(s) for both the print and online format.

References

[1] A. Vakil and N. Engheta, “Transformation optics using graphene,” *Science*, 2011, 332(6035): 1291–1294.

[2] J. Wang, J. Song, X. Mu, and M. Sun, “Optoelectronic and photoelectric properties and applications of graphene-based nanostructures,” *Materials Today Physics*, 2020, 13, 100196.

[3] H. Chen, H. Zhang, M. Liu, Y. Zhao, X. Guo, and Y. Zhang, “Realization of tunable plasmon-induced transparency by bright-bright mode coupling in Dirac semimetals,” *Optical Materials Express*, 2017, 7(9): 3397–3407.

[4] D. F. Phillips, A. Fleischhauer, A. Mair, R. L. Walsworth, and M. D. Lukin, “Storage of light in atomic vapor,” *Physical Review Letters*, 2001, 86(5): 783–786.

[5] T. Nurmohammadi, K. Abbasian, and R. Yadipour, “Ultra-fast all-optical plasmonic switching in near infra-red spectrum using a Kerr nonlinear ring resonator,” *Optics Communications*, 2018, 410: 142–147.

[6] F. Chen, H. Zhang, L. Sun, and C. Yu, “Tunable plasmonic properties of graphene ribbon for hypersensitive nanosensing,” *Optik*, 2019, 196: 163139.

[7] Z. Chen, L. Yu, L. Wang, G. Duan, Y. Zhao, and J. Xiao, “A refractive index nanosensor based on Fano resonance in the plasmonic waveguide system,” *IEEE Photonics Technology Letters*, 2015, 27(16): 1695–1698.

[8] Q. Lu, Z. Wang, Q. Huang, W. Jiang, Z. Wu, Y. Wang, *et al*., “Plasmon-induced transparency and high-performance slow light in a plasmonic single-mode and two-mode resonators coupled system,” *Journal of Lightwave Technology*, 2017, 35(9): 1710–1717.

[9] S. Wang, T. Zhao, S. Yu, and W. Ma, “High-performance nano-sensing and slow-light applications based on tunable multiple Fano resonances and EIT-like effects in coupled plasmonic resonator system,” *IEEE Access*, 2020, 8: 40599–40611.

[10] Y. Cui and C. Zeng, “All-optical EIT-like phenomenon in plasmonic stub waveguide with ring resonator,” *Optics Communications*, 2013, 297: 190–193.

[11] R. Zhou, J. Ding, B. Arigong, Y. Lin, and H. Zhang, “Broadband monopole optical nano-antennas,” in *Conference on Terahertz, RF, Millimeter, and*

Submillimeter-Wave Technology and Applications VII, San Francisco, 2014, pp. 93–98.

[12] A. Furusawa and N. Takei, "Quantum teleportation for continuous variables and related quantum information processing," *Physics Reports*, 2007, 443(3): 97–119.

[13] S. Zhang, D. A. Genov, Y. Wang, M. Liu, and X. Zhang, "Plasmon-induced transparency in metamaterials," *Physical Review Letters*, 2008, 101(4): 047401.

[14] A. K. Geim and K. S. Novoselov, "The rise of graphene," *Nature Materials*, 2007, 6(3): 183–191.

[15] S. Chen, J. Li, Z. Guo, L. Chen, K. Wen, P. Xu, *et al.*, "Dynamically tunable plasmon-induced transparency effect based on graphene metasurfaces," *Journal of Physics D – Applied Physics*, 2022, 55(11): 115105.

[16] B. Zhang, H. Li, H. Xu, M. Zhao, C. Xiong, C. Liu, *et al.*, "Absorption and slow-light analysis based on tunable plasmon-induced transparency in patterned graphene metamaterial," *Optics Express*, 2019, 27(3): 3598–3608.

[17] J. Li, J. Weng, J. Li, S. Chen, Z. Guo, P. Xu, *et al.*, "Dynamic manipulation of plasmon induced transparency with parallel-orthometric graphene strips structure," *Results in Physics*, 2022, 40: 105816.

[18] B. Zhang, H. Xu, M. Zhao, C. Xiong, C. Liu, B. Zeng, *et al.*, "Triple mode coupling effect and dynamic tuning based on the zipper-type graphene terahertz metamaterial," *Journal of Physics D – Applied Physics*, 2020, 53(13): 135105.

[19] M. Zhao, H. Xu, C. Xiong, B. Zhang, C. Liu, W. Xie, *et al.*, "Tunable slow light effect based on dual plasmon induced transparency in terahertz planar patterned graphene structure," *Results in Physics*, 2019, 15: 102796.

[20] J. Li, J. Weng, J. Li, S. Chen, Z. Guo, P. Xu, *et al.*, "Switchable triple plasmon-induced transparency in graphene sandwich metamaterial structures," *Journal of Physics D – Applied Physics*, 2022, 55(44): 445101.

[21] M. Li, C. Xiong, C. Liu, B. Zeng, B. Ruan, B. Zhang, *et al.*, "Terahertz plasmonic sensing based on tunable multispectral plasmon-induced transparency and absorption in graphene metamaterials," *Journal of Physics D – Applied Physics*, 2021, 54(24): 245201.

[22] Z. Liu, X. Zhang, F. Zhou, X. Luo, Z. Zhang, Y. Qin, *et al.*, "Triple plasmon-induced transparency and optical switch desensitized to polarized light based on a mono-layer metamaterial," *Optics Express*, 2021, 29(9): 13949–13959.

[23] H. Xu, H. Xu, X. Yang, M. Li, H. Yu, Y. Cheng, *et al.*, "Polarization-sensitive asynchronous switch and notable slow-light based on tunable triple plasmon-induced transparency effect," *Physics Letters A*, 2024, 504: 129401.

[24] C. Xiong, L. Chao, B. Zeng, K. Wu, M. Li, B. Ruan, *et al.*, "Dynamically controllable multi-switch and slow light based on a pyramid-shaped monolayer graphene metamaterial," *Physical Chemistry Chemical Physics*, 2021, 23(6): 3949–3962.

[25] X. Zhang, Z. Liu, Z. Zhang, E. Gao, F. Zhou, X. Luo, *et al.*, "Photoelectric switch and triple-mode frequency modulator based on dual-PIT in the multilayer patterned graphene metamaterial," *Journal of the Optical Society of America A – Optics Image Science, and Vision*, 2020, 37(6): 1002–1007.

[26] X. Zhang, Z. Liu, Z. Zhang, E. Gao, X. Luo, F. Zhou, *et al.*, "Polarization-sensitive triple plasmon-induced transparency with synchronous and asynchronous switching based on monolayer graphene metamaterials," *Optics Express*, 2020, 28(24): 36771–36783.

[27] M. Li, H. Xu, H. Xu, X. Yang, H. Yu, Y. Cheng, *et al.*, "Multi-frequency modulator of dual plasma-induced transparency in graphene-based metasurface," *Optics Communications*, 2024, 554: 130175.

[28] X. Jiang, D. Chen, Z. Zhang, J. Huang, K. Wen, J. He, *et al.*, "Dual-channel optical switch, refractive index sensor and slow light device based on a graphene metasurface," *Optics Express*, 2020, 28(23): 34079–34092.

[29] B. Ruan, Q. You, J. Zhu, L. Wu, J. Guo, X. Dai, *et al.*, "Fano resonance in double waveguides with graphene for ultrasensitive biosensor," *Optics Express*, 2018, 26(13): 16884–16892.

[30] H. Xu, M. Li, X. Yang, H. Xu, and Z. Chen, "Dynamically tunable terahertz slow light device based on triple plasmonic induced transparency," *Scientia Sinica – Physica Mechanica & Astronomica*, 2024, 54(3): 234211.

[31] J. Y. Zhang, J. Y. Li, S. X. Chen, K. H. Wen, and W. J. Liu, "Quadruple plasmon-induced transparency and dynamic tuning based on bilayer graphene terahertz metamaterial," *Nanomaterials*, 2023, 13(17): 2474.

[32] S. Zheng, Q. Zhao, L. Peng, and X. Jiang, "Tunable plasmon induced transparency with high transmittance in a two-layer graphene structure," *Results in Physics*, 2021, 23: 104040.

[33] Z. G. Dong, H. Liu, M. X. Xu, T. Li, S. M. Wang, S. N. Zhu, *et al.*, "Plasmonically induced transparent magnetic resonance in a metallic metamaterial composed of asymmetric double bars," *Optics Express*, 2010, 18(17): 18229–18234.

[34] L. Ju, B. Geng, J. Horng, C. Girit, M. Martin, Z. Hao, *et al.*, "Graphene plasmonics for tunable terahertz metamaterials," *Nature Nanotechnology*, 2011, 6(10): 630–634.

[35] E. Gao, H. Li, Z. Liu, C. Xiong, C. Liu, B. Ruan, *et al.*, "Terahertz multifunction switch and optical

storage based on triple plasmon-induced transparency on a single-layer patterned graphene metasurface," *Optics Express*, 2020, 28(26): 40013–40023.

[36] C. H. Gan, H. S. Chu, and E. P. Li, "Synthesis of highly confined surface plasmon modes with doped graphene sheets in the midinfrared and terahertz frequencies," *Physical Review B*, 2012, 85(12): 125431.

[37] K. L. Tsakmakidis, L. Shen, S. A. Schulz, X. Zheng, J. Upham, X. Deng, *et al.*, "Breaking Lorentz reciprocity to overcome the time-bandwidth limit in physics and engineering," *Science*, 2017, 356(6344): 1260–1264.

[38] H. A. Haus and W. Huang, "Coupled-mode theory," *Proceedings of the IEEE*, 1991, 79(10): 1505–1518.

[39] H. Xu, M. Zhao, M. Zheng, C. Xiong, B. Zhan, Y. Peng, *et al.*, "Dual plasmon-induced transparency and slow light effect in monolayer graphene structure with rectangular defects," *Journal of Physics D – Applied Physics*, 2019, 52(2): 025104.

[40] Y. Li, Y. Xu, J. Jiang, L. Ren, S. Cheng, W. Yang, *et al.*, "Quadruple plasmon-induced transparency and tunable multi-frequency switch in monolayer graphene terahertz metamaterial," *Journal of Physics D – Applied Physics*, 2022, 55(15): 155101.

[41] Z. Liu, E. Gao, X. Zhang, H. Li, H. Xu, Z. Zhang, *et al.*, "Terahertz electro-optical multi-functional modulator and its coupling mechanisms based on upper-layer double graphene ribbons and lower-layer a graphene strip," *New Journal of Physics*, 2020, 22(5): 053039.

[42] S. J. Koester, H. Li, and M. Li, "Switching energy limits of waveguide-coupled graphene-on-graphene optical modulators," *Optics Express*, 2012. 20(18): 20330–20341.

[43] Q. Meng, F. Chen, Y. Xu, S. Cheng, W. Yang, D. Yao, *et al.*, "Multi-frequency polarization and electro-optical modulator based on triple plasmon-induced transparency in monolayer graphene metamaterials," *Diamond and Related Materials*, 2023, 138: 110216.

[44] Q. Meng, F. Chen, Y. Xu, S. Cheng, W. Yang, D. Yao, *et al.*, "Tunable terahertz double plasmon induced-transparency based on monolayer patterned graphene structure," *Photonics and Nanostructures – Fundamentals and Applications*, 2023, 54: 101132.

[45] X. Guo, J. Cong, and C. Li, "Dynamic tunable multiple plasmon induced transparency sensor and optical switch in dual-polarization excitation in a terahertz graphene metamaterial," *Optics Communications*, 2024, 551: 130058.

[46] C. Fan, P. Ren, W. Jia, Y. Jia, and J. Wang, "Tunable plasmon induced transparency in patterned graphene metamaterial with different carrier mobility," *Superlattices and Microstructures*, 2019, 136: 106295.

[47] K. Wang, W. H. Fan, X. Chen, C. Song, and X. Q. Jiang, "Graphene based polarization independent Fano resonance at terahertz for tunable sensing at nanoscale," *Optics Communications*, 2019, 439: 61–65.

[48] M. Chen and Z. Xiao, "Metal-graphene hybrid terahertz metamaterial based on dynamically switchable electromagnetically induced transparency effect and its sensing performance," *Diamond and Related Materials*, 2022, 124: 108935.

[49] M. R. Forouzeshfard, S. Ghafari, and Z. Vafapour, "Solute concentration sensing in two aqueous solution using an optical metamaterial sensor," *Journal of Luminescence*, 2021, 230: 117734.

[50] J. Zhu and J. Xiong, "Tunable terahertz graphene metamaterial optical switches and sensors based on plasma-induced transparency," *Measurement*, 2023, 220: 113302.